ACS APPLIED ENERGY MATERIALS

www.acsaem.org Article

Mechanical Pulverization of Co-Free Nickel-Rich Cathodes for Improved High-Voltage Cycling of Lithium-Ion Batteries

Ryan Brow,* Anthony Donakowski, Alex Mesnier, Drew J. Pereira, K. Xerxes Steirer, Shriram Santhanagopalan,* and Arumugam Manthiram*

Cite This: *ACS Appl. Energy Mater.* 2022, 5, 6996−7005 Read Online

ACCESS | Metrics & More | Article Recommendations | Supporting Information

ABSTRACT: Nickel-rich cathode materials are quickly becoming the next commercial cathode for electric vehicles; however, their long-term cycle life retention and air stability remain a barrier to the use of these lower-cost, higher-energy density materials. Surface reactivity and mechanical degradation, especially at high voltages, remain two issues that impede these material's commercialization. While surface treatments have shown great promise in reducing surface reactivity, mechanical degradation or "cathode cracking" persists yet. In the present work, $LiNi_{0.9}Mn_{0.05}Al_{0.05}O_2$ (NMA) cathode materials are first pulverized into their primary particle constituents and then coated with lithium phosphate via solution-based chemistry with varying concentrations of phosphoric acid. The cathodes are characterized using energy-dispersive X-ray spectroscopy, X-ray photoelectron spectroscopy, transmission electron microscopy, electrochemical impedance spectroscopy, and electrochemical cycling. After 100 cycles, the pulverized NMA cathodes coated using the lowest concentration of phosphoric acid show delayed voltage decay and double the discharge capacity compared to the pristine material in full cells during high-voltage cycling.

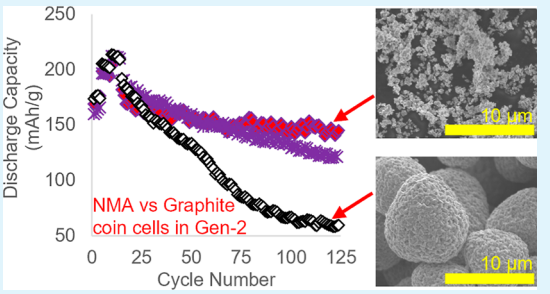

KEYWORDS: *cathode, nickel-rich, cathode cracking, lithium-ion, coating, high voltage*

INTRODUCTION

Lithium-ion batteries are at the forefront of the coming electric vehicle revolution due to their relatively high specific and volumetric capacities, longevity, and plummeting cost.[1−3] A typical commercial battery will have a transition-metal (TM) oxide as its cathode, with $LiCoO_2$ being the first widely available and most successful metal oxide cathode. However, this material suffers from low practical capacity, safety concerns, unreliable raw material sourcing, and high cost.[4−7] Therefore, there has been an effort to both decrease the cost and increase the capacity of these cathodes by replacing Co with Ni to ever-greater extents.[8]

Nickel can more readily oxidize to its $Ni^{3+/4+}$ oxidation state because its energy band does not overlap with that of the O^{2-}:2p band in TM oxide cathodes. The same cannot be said of $Co^{3+/4+}$ because its overlap with the O^{2-}:2p band causes oxygen release from the TM oxide structure when $Li_{1-x}CoO_2$ is delithiated beyond 50% ($x > 0.5$) on charging,[9] limiting its practical capacity to 140 mA h/g.[10,11] Nickel is also cheaper and has more reliable raw material sourcing.[12] Unfortunately, these nickel-rich cathode materials experience cycle life reduction due to several factors including electrolyte-induced surface nickel reduction,[13] particle fracture,[13] air instability, and cation mixing.[14] Ni^{4+} can undergo reduction by carbonate electrolytes and form NiO-type rock-salt phase impurities, which reduce the available active sites and impede facile lithium-ion transport.[13] Particle fracture is induced between weakly bound primary particles in the secondary particle structure due to anisotropic lattice expansion/contraction during lithiation/delithiation. This leads to fracturing at the grain boundary and infiltration of the electrolyte, which reduces Ni^{4+} and leads to more phase impurity and active-site loss.[15] Residual lithium compounds (Li_2O, LiOH, and Li_2CO_3) can form on nickel-rich cathode surfaces via exposure to air during material synthesis and electrode processing causing the gelation of electrode slurry and gas generation on cycling.[14] Finally, due to similar radii of Ni^{2+} (0.69 Å) and Li^+ (0.76 Å), Ni^{2+} can be incorporated into active sites and reduce lithium transport in the layered structure.[16]

To mitigate the above issues, several strategies have been attempted: doping,[17−19] surface modification,[20] surface modification via intentional electrolyte additive decomposition,[21−23] process refinement,[24,25] TM concentration gradient,[26] core−shell structures,[27] grain boundary tailoring,[28] and single-crystalline morphology.[29,30] Individually, these

Received: February 28, 2022
Accepted: May 19, 2022
Published: June 8, 2022

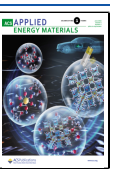

modifications fail to generate nickel-rich cathode materials with optimum cycle life retention and air stability for commercial use. Particle cracking may still occur with high-voltage cycling, slowly degrading performance, and air instability allows residual lithium compounds to form during material synthesis and electrode production.

In this work, two mitigation strategies have been combined to limit particle fracture and surface degradation caused by air instability. First, Co-free Ni-rich NMA ($LiNi_{0.9}Mn_{0.05}Al_{0.05}O_2$), which demonstrates excellent capacity retention with moderate voltage windows,[31] was ball-milled to effectively "pre-crack" the secondary particles into their primary constituents or single crystallites. Currently, the synthesis parameters of NMA are rather constrained due to its high aluminum content, which can cause secondary phases to appear during calcination.[31] This limits the possibility of growing single-crystalline NMA. Ball milling allows the use of the NMA material without the limitations of its secondary structure facture as stated above. Second, these primary particles were coated with lithium phosphate using varying concentrations of phosphoric acid. This manufacturing-friendly, solution-based chemistry protects the primary particles from detrimental side reactions potentially exaggerated by its high surface-to-volume ratio. With the appropriate concentration of phosphoric acid, the pre-cracked cathode powders have a higher volumetric energy density and greater high voltage and air stability, with double the cycle life retention in full cells cycled at high voltages.

EXPERIMENTAL SECTION

Materials Synthesis. The spherical $Ni_{0.9}Mn_{0.05}Al_{0.05}(OH)_2$ precursor of 10−12 μm diameter was synthesized through coprecipitation of $NiSO_4{\cdot}6H_2O$, $MnSO_4{\cdot}H_2O$, and $Al(NO_3)_3{\cdot}9H_2O$, as described in a previous publication.[31] Briefly, aqueous solutions of the metal-ion sources were prepared with appropriate molar ratios and pumped into a 10 L continuously stirred tank reactor under a nitrogen atmosphere. Aqueous solutions of KOH and NH_4OH were also fed to the reactor to control the pH and precipitation rate. The reactor temperature, pH, and stir rate were carefully controlled for the extent of coprecipitation. Once complete, the resultant $Ni_{0.9}Mn_{0.05}Al_{0.05}(OH)_2$ was washed thoroughly, vacuum-filtered, and allowed to dry overnight. To synthesize $LiNi_{0.9}Mn_{0.05}Al_{0.05}O_2$ (NMA), the coprecipitated mixed-metal hydroxide was mixed with $LiOH{\cdot}H_2O$ in a molar ratio of 1:1.01 and subsequently calcined under flowing oxygen at 760 °C for 12 h.

Ball Milling. A high-energy, planetary ball milling process was employed to pulverize the cathode active materials into a semiuniform nanostructure, as previously investigated using NMC532 ($LiNi_{0.5}Mn_{0.3}Co_{0.2}O_2$).[32] A 1:10 weight ratio of cathode active materials (5 g NMA) and ZrO_2 spheres (50 g of 3 mm diameter) were inserted into a ZrO_2 vessel (25 ml) and sealed in an Argon atmosphere. The chamber was fixed inside a Retsch PM 200 planetary mill and operated at a speed of 450 rpm. The milling procedure included grinding and rest times of 60 and 20 s, respectively, and included a reversal of rotation direction after each rest. An operational time of 75 min was used to obtain nanoscale primary particles as assessed by scanning electron microscopy (SEM) (see below). The specific surface area and pore size distribution of the samples were measured in a Micromeritics ASAP 2020 apparatus at 77 K in N_2, using sample sizes of 346 and 1335 mg for the ball-milled and pristine cathodes, respectively. The relative pressure regimes for the Brunauer−Emmet−Teller (BET) analysis were chosen according to the criteria for evaluating the BET surface areas of microporous materials.[32] Tap density was measured using an Anton Paar Dual Autotap with a tap height of 3 mm and 260/min tap rate. The cylinder was tapped until density stabilized after approximately 5000 taps.

Phosphate Coating. Lithium phosphate coatings were performed using a diffusion-controlled reaction with phosphoric acid in an ethanol solution. A similar method for performing the phosphate coatings was described previously.[33] Phosphoric acid (Sigma-Aldrich) and pristine NMA of varying weight ratios were mixed with anhydrous ethanol (Sigma-Aldrich) in an argon glovebox. The solution was stirred and brought to 85 °C until the solvent evaporated. The dried powder was then loaded into a tube furnace and heated to 500 °C for 5 h in air.

Cell Fabrication and Electrochemical Testing. The coated and uncoated NMA (90 wt %) were weighed in air and mixed with carbon black (5 wt %) and PVDF from MTI Corp. (5 wt %) in NMP (Sigma-Aldrich) for 3 min using a speed mixer. The slurry was then coated onto an aluminum foil in air using a doctor blade and then placed in a vacuum oven to be dried overnight at 100 °C. All electrodes were fabricated with an approximate energy-to-area density of 1 mA h/cm^2. The electrodes were weighed and assembled into either half or full coin cells in an argon glovebox with <0.1 ppm water and O_2. Graphite and lithium metal were obtained from MTI Corp. All cells were assembled using 60 μL of the Gen-2 electrolyte [comprising 1.2 M lithium hexafluorophosphate ($LiPF_6$) in a mixed solvent of ethylene carbonate ethyl methyl carbonate (3:7 by weight) purchased from Tomiyama)] and cycled at room temperature. Charge and discharge steps were all performed under constant current conditions without any constant voltage step. Formation occurred at C/10 (1 C = 180 mA h/g) charge/discharge rates and subsequent cycling occurred at C/3. A rest time of 15 min was allowed between charge and discharge.

X-Ray Photoelectron Spectroscopy. X-Ray photoelectron spectroscopy (XPS) was performed using a Scientia Omicron HiPP-3 system using Monochromatic Al Kα X-rays with 1496.7 eV excitation energy. The X-rays liberate core level electrons from an 800 μm diameter spot. The kinetic energy photoelectrons are then measured and via the photoelectric effect, a plot of photoelectron intensity versus binding energy is obtained. Equipment was calibrated to Au $4f_{7/2}$ = 83.98 eV using an argon sputter-cleaned Au foil. Each sample was exposed to air for 60 min and then analyzed using 200 eV pass energy and a 500 μm slit size in ultra-high vacuum conditions ~1 × 10^{-7} mBar. For all scans, the adventitious C−C peak was calibrated to 284.6 eV.

X-Ray Diffraction. X-Ray diffraction (XRD) data were acquired using a PANanalytical Empyrean detector using Cu radiation. The samples were prepped on a glass slide and ground into a fine powder using a razor blade. Gonio 2-theta scans were taken using a divergence slit of one-fourth, an anti-scatter slit of 1, and a 1 mm mask. Rietveld refinement was performed using High-Score Plus software and pattern matched using the ICSD database. The lattice parameters, site occupancy, sample alignment, roughness, and scale factor were refined to fit the spectra.

RESULTS AND DISCUSSION

Ball Milling and Li_3PO_4 Coating. The NMA active material's secondary particles were mechanically pulverized, or pre-cracked, into primary particles or single crystallites using the ball milling technique. A set gravimetric ratio of cathode active material powder and ceramic balls were placed in a ceramic chamber and run through a planetary ball mill over a set revolution speed and length of time to achieve the appropriate pulverization for this study as assessed by SEM (Figure 1). Previously, Kim et al. employed a high-energy ball milling method to prepare nanostructured electrodes with much smaller particle sizes, ultimately leading to a much higher first charge/discharge capacity compared to bulk-type electrodes.[32] Stein et al. performed a parametric study of the effect of ball milling times, speeds, and compositions and found it possible to tune the cathode active material particle size. They also discovered that high milling speeds and long milling times resulted in smaller crystallite sizes; however, they found that

https://doi.org/10.1021/acsaem.2c00606
ACS Appl. Energy Mater. 2022, 5, 6996−7005

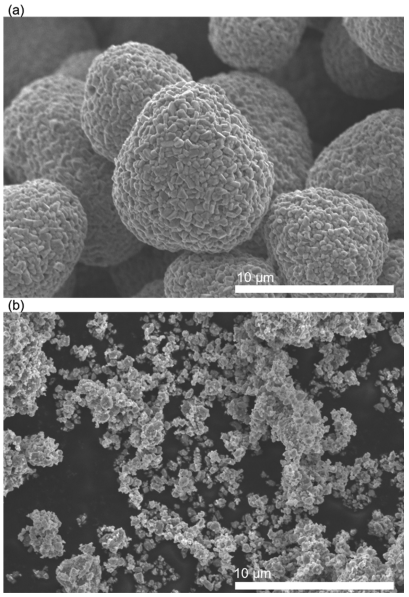

Figure 1. Pristine NMA's secondary particle structure (a) and NMA after mechanical pulverization using the ball mill technique (b) as seen in SEM. Images are the same scale.

the electrochemical performance suffers.[34] Pan et al. uncovered similar results and suggested that electrochemical degradation is strongly correlated with damage to the lamellar structure of cathode particles induced by milling and lithium carbonate formation.[35] In our study, ball milling takes place in an inert atmosphere to avoid the formation of residual lithium compounds. A 1:10 weight ratio of NMA active material to 3 mm zirconia milling media milled at 450 rpm for 75 min achieved the desired effect of pulverizing the particles' secondary structure as evaluated by SEM (Figure 1).

XRD Analysis. Phase purity of the ball-milled NMA (BM-NMA) was compared to the pristine material (P-NMA) via XRD (Figure 2) and reveals that both samples have a hexagonal α-$NaFeO_2$-type structure of the $R\bar{3}m$ space group and neither sample shows any phase impurity. Both samples show splitting of the (018)/(110) and (006)/(012) peaks, signifying a high degree of crystallinity, although a larger FWHM of these doublets and the (003) peak for the BM-NMA suggests a smaller crystallite size caused by the pulverization of some of the primary particles (Figure S1, Supporting Information). Crystallite sizes based on the Scherrer equation using the (003) diffraction peak yields 51 nm for the pristine and 44 nm for the ball-milled material. Lattice parameters for both the a and c axes show negligible changes based on Rietveld refinement (Table S1, Supporting Information). Rietveld refinement yields lithium/nickel cations mixing for the P-NMA and the BM-NMA of 3.6 and 4.3%, whereas the integrated intensity ratios of $I(003)/I(104)$ yields 1.299 and 1.263, respectively.

Mechanical pulverization of the NMA secondary structure increases tap density mildly and greatly increases the material's surface area, the measured tap density and BET surface areas are 2.02 and 2.07 g/cm^3 and 0.66 and 4.49 m^2/g for the P-NMA and BM-NMA, respectively. To avoid the negative effects of having a large cathode surface area exposed to the electrolyte during electrochemical testing, a lithium phosphate coating was applied to the surface of both the ball milled and the non-ball milled material. Sun et al. used phosphoric acid to

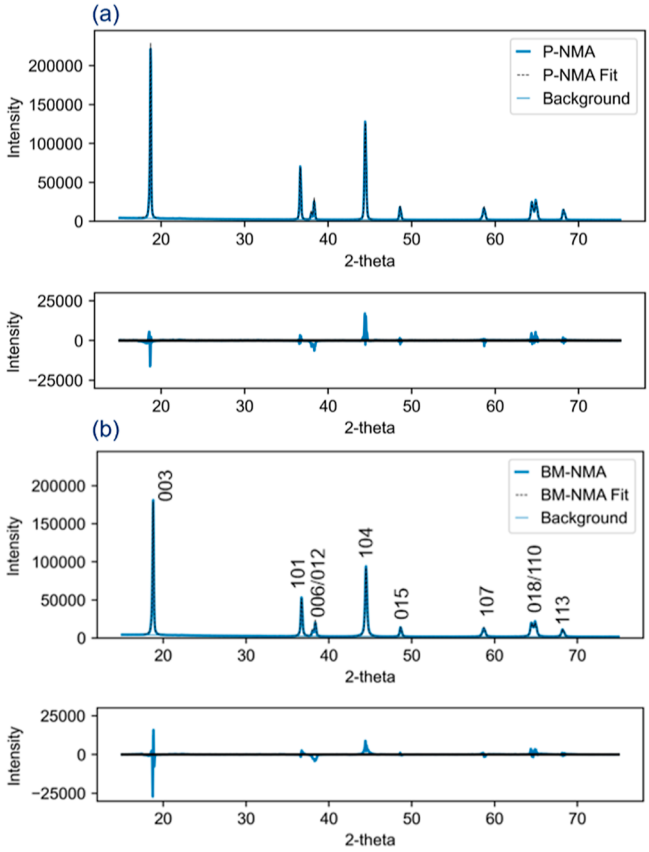

Figure 2. XRD data comparing pristine NMA (a) and ball-milled NMA (b) with their corresponding Rietveld mismatch.

create a 10 nm thick lithium phosphate layer and proposed that lithium carbonate and lithium hydroxide residual compounds are consumed to form lithium phosphate on heating.[33] The increased capacity retention of the lithium phosphate-coated material can be attributed to lithium phosphate's high ionic conductivity and its voltage stability (0−4.7 V) (all voltages are V vs Li/Li$^+$),[36,37] whereas the residual lithium compounds impede facile lithium-ion diffusion.[38] The lithium phosphate coating method has been reported previously.[33,39] Samples were placed in a beaker containing anhydrous ethanol and phosphoric acid of various concentrations. Starting concentrations (1 wt %) were determined by Sun et al. and decreased to 0.4 wt % with the goal of a thinner lithium phosphate coating.[33] The ethanol was evaporated at 80 °C, while the solution was stirred and the resulting powder was baked at 500 °C in air.

Transmission Electron Microscopy/Energy-Dispersive X-Ray Spectroscopy. To confirm that lithium phosphate was successfully formed on the NMA's surface, and to gain insights into the coating thickness and uniformity, transmission electron microscopy (TEM) images were obtained for the UTC-BM-NMA (Table 1) material (Figure 3). The coating thickness ranges from barely detectable to 7 nm, does not appear to be conformal, and individual particles seem to have a large variation in coating thickness. Energy-dispersive X-ray spectroscopy (EDX) analysis shown in Figure 4 was also used to identify the lithium phosphate coating and its uniformity. The k-alpha signals of the ball-milled and lithium phosphate-coated samples show a clear phosphorous signal. Spatially, the peak counts Al, Mn, Ni, and P closely align, and the particle

https://doi.org/10.1021/acsaem.2c00606
ACS Appl. Energy Mater. 2022, 5, 6996−7005

Table 1. Sample Names and Their Brief Description[a]

sample name	description	ball milled	lithium phosphate coating (NMA wt/phosphoric acid wt)
P-NMA	pristine NMA	no	no
BM-NMA	milled NMA	yes	no
C-NMA	coated NMA	no	yes (100:1)
C-BM-NMA	milled and coated NMA	yes	yes (100:1)
TC-NMA	thinly coated NMA	no	yes (175:1)
TC-BM-NMA	milled and thinly coated NMA	yes	yes (175:1)
UTC-NMA	ultra-thinly coated NMA	no	yes (230:1)
UTC-BM-NMA	milled and ultra-thinly coated NMA	yes	yes (230:1)

[a]All milled samples were milled using the process outlined in the Experimental Section. All coated samples were coated with lithium phosphate using varying concentrations of phosphoric acid during the solution coating to apply ever thinner lithium phosphate coatings.

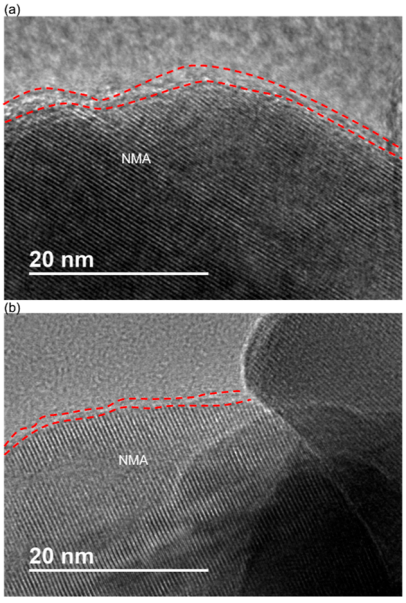

Figure 3. Lithium phosphate-coated NMA (a,b). The layered structure of the NMA can clearly be seen and a thin, nonconformal, coating of approximately 3 nm is outlined in red.

shape can be delineated from the scan, indicating that most of the NMA particle has at least some phosphate coating. There are clear regions with higher P counts compared with the bulk metal oxide suggesting a nonuniform coating, in agreement with the TEM scan. Similar results were obtained by Sahni et al.[39] Although the coating thickness shows large variations, there appears to be P present in all regions where the TMs are found, signifying at least partial protection for large portions of the NMA surface.

XPS Analysis. Samples of coated and uncoated NMA were exposed to air for 60 min to allow for partial growth of residual lithium species and analyzed with XPS prior to cycling. See Table 1 for sample names and a brief description. The O 1S XPS peak for the uncoated, BM Li_3PO_4-coated, and the non-BM Li_3PO_4-coated NMA hint at possible explanations for the increased capacity retention of the coated NMA material (Figure 5). The characteristic Li_2CO_3 peak at 532 eV can be seen in all three samples and is shifted ~0.43 eV for the coated samples toward the lithium phosphate O 1S peak. Panels B and C both show the emergence of a fifth oxygen peak at 531.5 eV, which corresponds to lithium phosphate and is corroborated by phosphate peaks at 133.6 eV in the P2p scans (Figure 5d). The lattice oxygen (M−O) peak is seen as a shoulder in the uncoated P-NMA sample and as a distinct peak in the Li_3PO_4 samples. It can be speculated that the decreased peak area of LiOH in the UTC-BM-NMA and UTC-NMA accounts for the change in the shape of the M−O peak envelope as the LiOH peak area falls from 29% in P-NMA of the total area to 17 and 3.1% for UTC-BM-NMA and UTC-NMA samples, respectively. The M−O peak is also shielded for the P-NMA due to the uncoated sample having ~9% more Li_2CO_3 and ~12−27% more LiOH than the UTC-BM-NMA and UTC-NMA samples, respectively. Indeed, the deconvoluted peak ratios of CO_3^{2-}/MO and OH^-/MO (Table 2) suggest that the uncoated sample has more residual lithium compounds, and this supports the assertion by Sun et al. that the phosphoric acid consumes these species to form Li_3PO_4.[33] When comparing the three ratios in Table 2 between the UTC-NMA and P-NMA, the high value for CO_3^{2-}/OH^- indicates that LiOH may be preferentially consumed during the coating process. That is, the lithium phosphate coating increases the air stability of the P-NMA by consuming the residual lithium compounds and converting them into an ionically conductive protective coating. Of the two coated samples, peak deconvolution suggests (Figure 5b,c) both have less Li_2CO_3 and LiOH than P-NMA with the BM material showing more Li_2CO_3 and LiOH. Because both the BM-NMA and the non-ball-milled UTC-NMA materials were exposed to the same concentration of phosphoric acid, the BM-NMA sample has less Li_3PO_4 and therefore, more residual lithium compounds due to its greater surface-area-to-volume ratio. The P 2p scans (Figure 5d) show a clear phosphorous signal near 134 eV for the UTC-NMA sample. The peak area ratios match an expected degeneracy of 2:1 between the 3/2 and 1/2 spin−

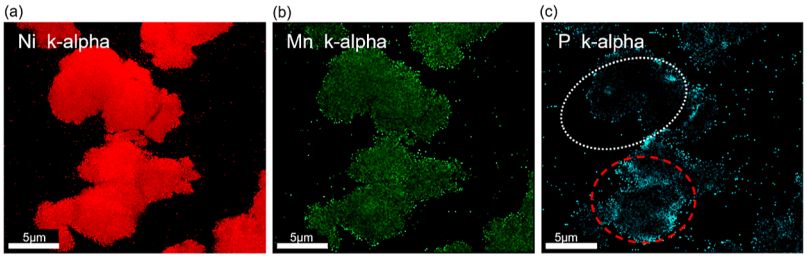

Figure 4. EDX image showing the k-alpha scans of nickel (a), manganese (b), and phosphorous(c). High P count density (red dash) and low P count density (white dot) indicate an uneven coating.

https://doi.org/10.1021/acsaem.2c00606
ACS Appl. Energy Mater. 2022, 5, 6996−7005

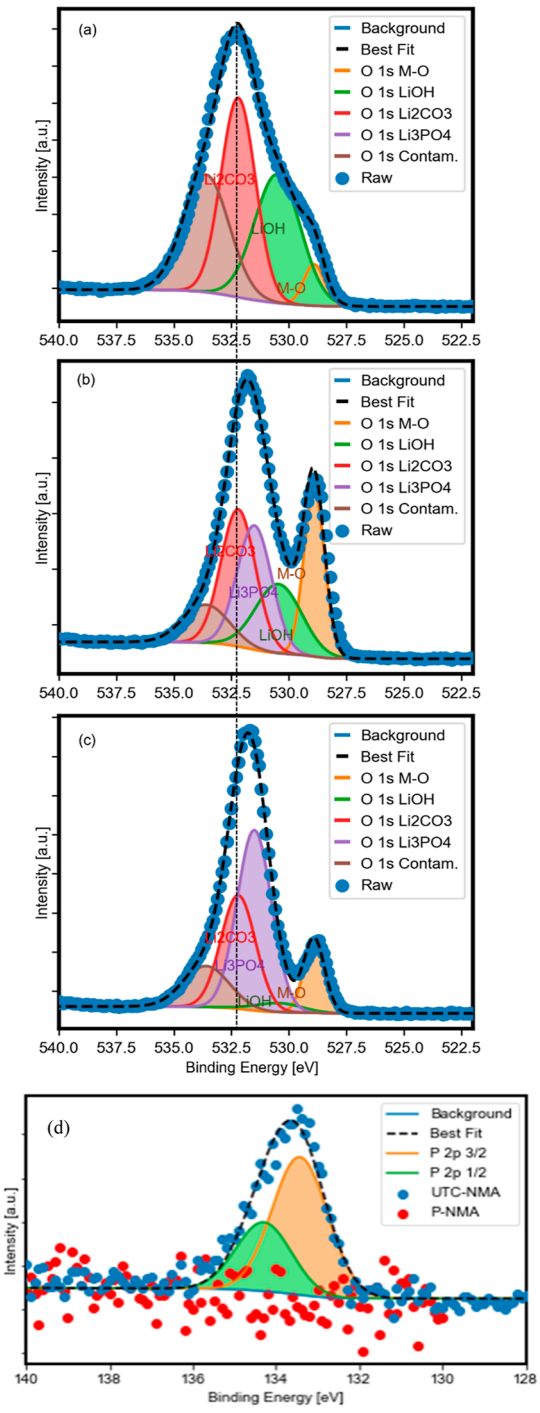

Figure 5. Oxygen 1s XPS scan data for P-NMA (a), UTC-BM-NMA (b), and UTC-NMA (c), showing a peak shift at 532.5 eV for samples coated with Li_3PO_4. Phosphorus P 2p scans showing metal phosphates on UTC-NMA and not P-NMA (d).

orbit coupling with the 3/2 peak at 133.4 eV and the 1/2 peak at 134.3 eV as expected for lithium phosphate.[39]

Electrochemical Impedance Spectroscopy. To analyze changes in the resistance of the coated material caused by the exposure to different concentrations of phosphoric acid during the solution-coating process (see Table 1), electrochemical impedance spectroscopy (EIS) was used after formation at a C/10 rate between 2.8 and 4.4 V in half coin cells (Figure 6a).

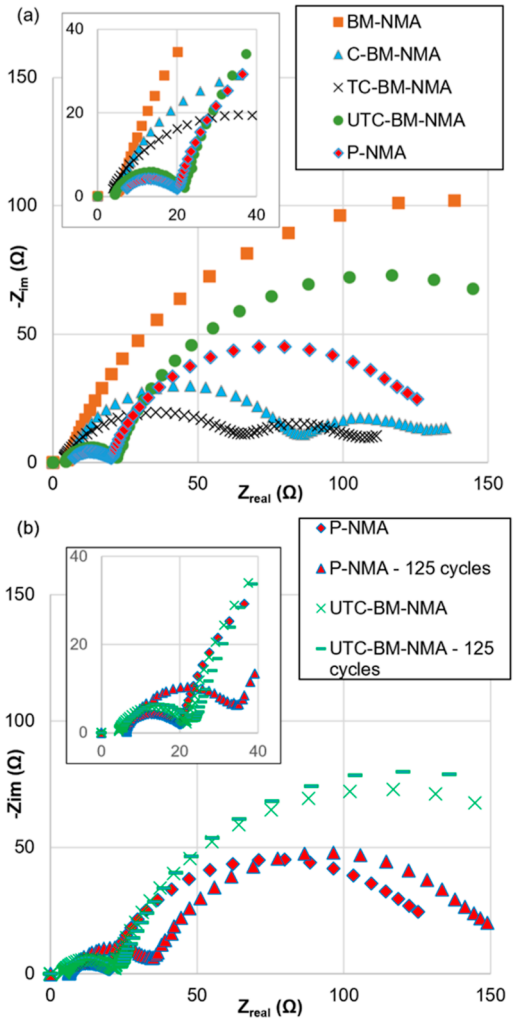

Figure 6. EIS data for P-NMA and ball-milled material with exposure to varying concentrations of phosphoric acid after formation (a). The R_{sf} of P-NMA increase between post-formation (a) and after 125 cycles (b). High-frequency region (inset).

A frequency range of 0.1Hz-1MHz was used with an AC perturbation of 10 mV. Measurements were taken at RT with approximately 50% SoC (based on the first discharge voltage profile). All cells show a solution resistance of 4 Ohm (±2

Table 2. Peak Ratios of Various O 1s Peaks Found in XPS Spectra (Figure 5)[a]

peak ratio	P-NMA (Figure 5a)	UTC-BM-NMA (Figure 5b)	UTC-NMA (Figure 5c)
CO_3^{2-}/OH^-	2.0	3.0	27
CO_3^{2-}/MO	6	1.4	3.0
OH^-/MO	3.0	0.5	0.1

[a]Peaks ratios suggest that the P-NMA samples contain more Li_2CO_3 and LiOH. The high value of CO_3/OH for the UTC-NMA sample suggests that LiOH is preferentially consumed during the coating process.

https://doi.org/10.1021/acsaem.2c00606
ACS Appl. Energy Mater. 2022, 5, 6996−7005

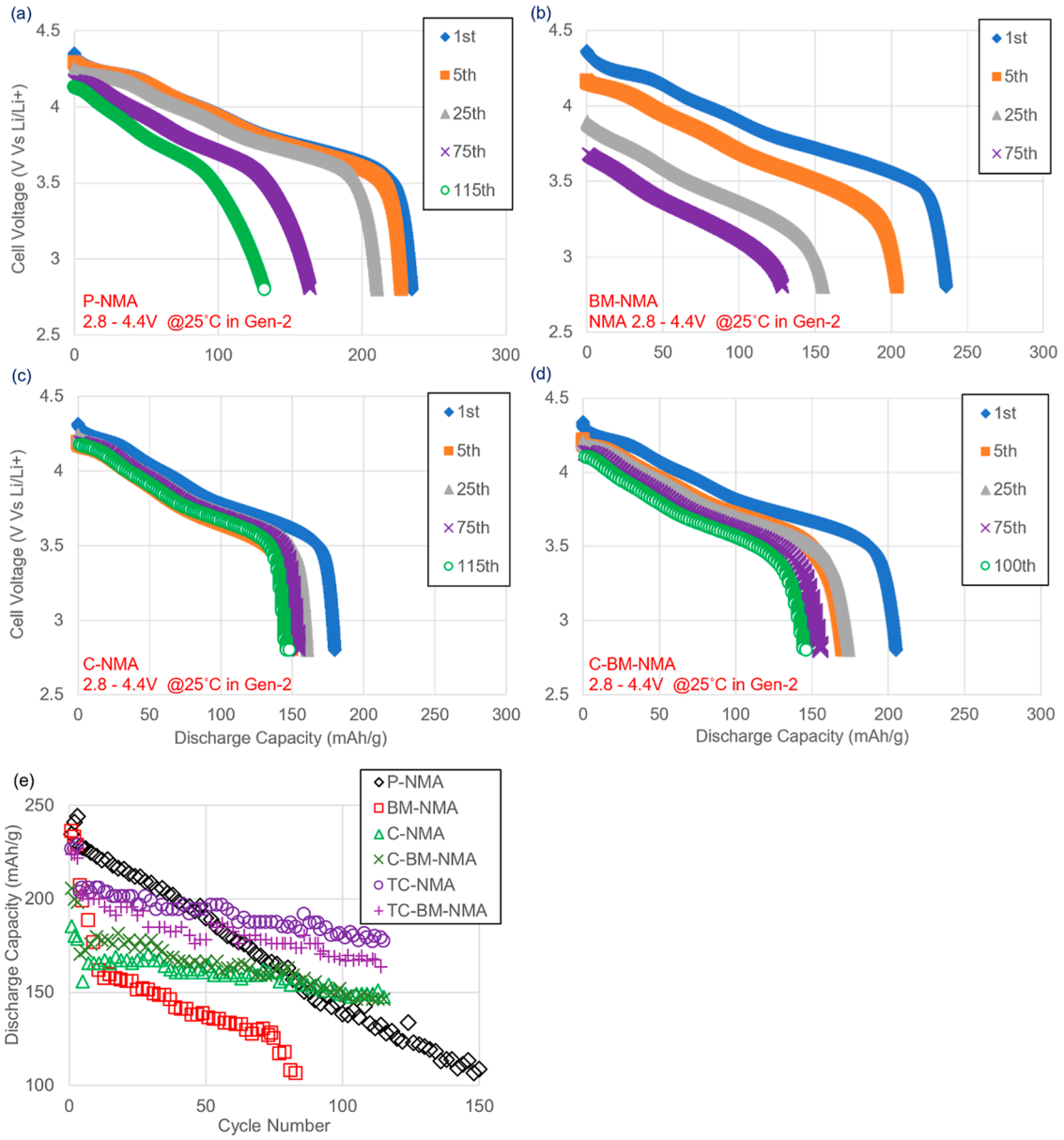

Figure 7. Initial cycling data for half cells containing P-NMA (a), BM-NMA (b), C-NMA (c), and C-BM-NMA (d). Capacity retention is increased when NMA is coated in lithium phosphate (e). Cells were formed at C/10 and cycled at C/3 thereafter.

Ohm). In coated nickel-rich cathodes, the first semicircle in the high-frequency region is assigned to the surface film resistance (R_{sf}) of the solid electrolyte interface (SEI).[40] As expected, the BM-NMA material shows the highest R_{sf} (280 Ohm) with its large surface area-to-volume ratio exposed to the electrolyte. The Li_3PO_4-coated samples have a lower R_{sf} resistance, which decreases along with the concentration of phosphoric acid, implying the lithium phosphate coatings are thinner with lower phosphoric acid concentrations. The R_{sf} for the UTC-BM-NMA (23 Ohm) is similar to the P-NMA (22 Ohm) after formation. The Nyquist plot for P-NMA, UTC-NMA, and UTC-BM-NMA after 125 cycles is shown in (Figure 6b). As the cells have cycled at high voltages, the R_{sf} of the P-NMA (42 Ohm) has increased by 20 Ohm, while the UTC-NMA and the UTC-BM-NMA R_{sf} remain unchanged. The R_{ct} for the P-NMA increases by 15% and remains the same for the UTC-BM-NMA after cycling. This could indicate an increase in the SEI thickness for the P-NMA or because a 50% SoC was determined by the voltage of the cell just after formation and could be caused by the difference in capacity between the P-NMA and UTC-BM-NMA cells making it difficult to perform EIS at the same SoC.[41]

Electrochemical Cycling. Initial cycling results for the P-NMA, BM-NMA, C-NMA, and C-BM-NMA materials are shown in Figure 7. See Table 1, for a list of sample names and their descriptions. The pristine NMA material that did not undergo any mechanical pulverization or coating is referred to as the "P-NMA". The sample that underwent lithium phosphate coating but no mechanical pulverization is "C-NMA" and the two balled-milled samples, one uncoated "BM-NMA" and one that was both coated and ball-milled "C-BM-NMA". Half coin cells using this material were first formed at C/10 and then cycled at C/3, all between 2.8 and 4.4 V (all voltages are V vs Li/Li^+) at RT. Initial results for the thicker of the phosphate coatings are seen in Figure 7. The pristine material has a capacity fade of 43% after 115 cycles and

https://doi.org/10.1021/acsaem.2c00606
ACS Appl. Energy Mater. 2022, 5, 6996−7005

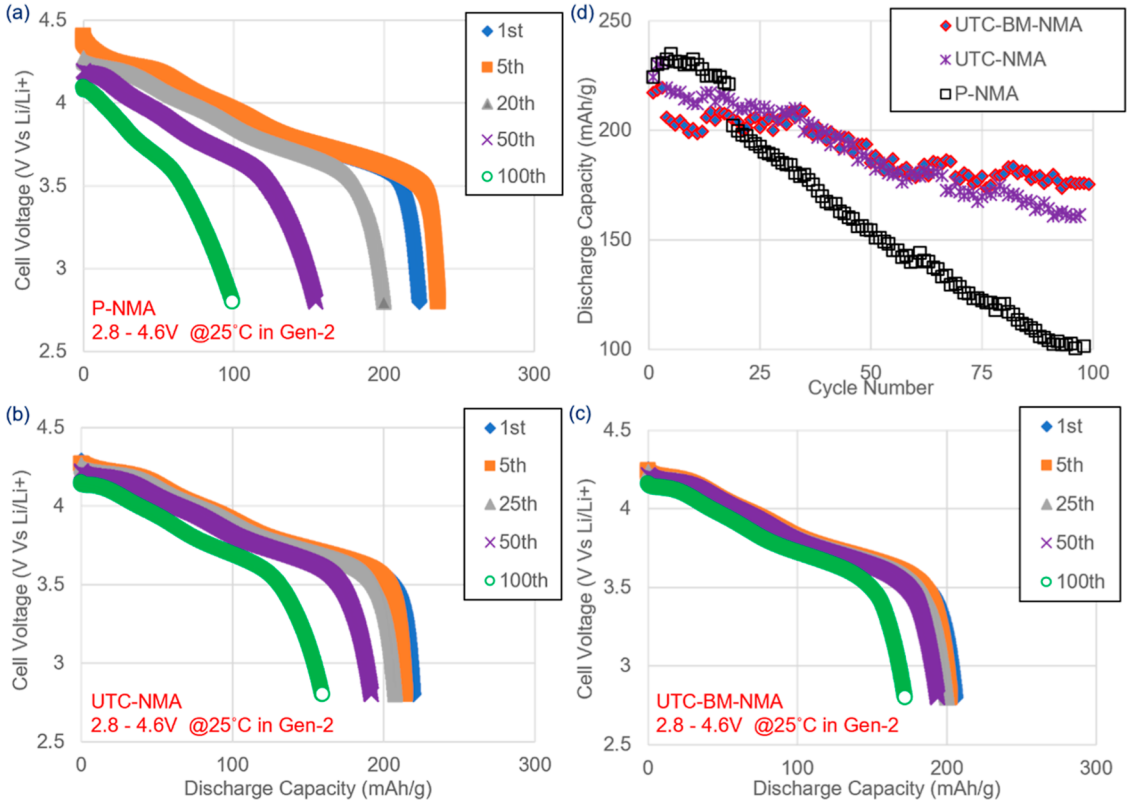

Figure 8. Half-cell cycling data for P-NMA (a), UTC-NMA (b), and UTC-BM-NMA (c). Discharge capacity versus cycle number for the same cells (d). The cells were formed from 2.8−4.4 V at C/10 for four cycles and the charged to 4.5 V between cycles 5−25 and 4.6 V after cycle 25 at C/3.

experiences a voltage decay of 0.23 V. The "C-NMA" has a capacity drop of 17% after 115 cycles and a voltage decay of 0.14 V. The C-BM-NMA sample experiences a capacity fade of 29% and a voltage decay of 0.23 V. The BM-NMA, having a large surface area-to-volume ratio experiences a large capacity fade and voltage decay as has been reported previously.[35] The difference in performance between BM-NMA and C-BM-NMA suggests that it is the surface area-to-volume ratio alone that causes the poor performance of the BM-NMA material and not crystalline reconstruction due to the mechanical forces experienced during milling. Both the C-NMA and C-BM-NMA have a lower than desired initial capacity, suggesting that lithium is consumed during the coating process.

To increase the initial capacity of the C-NMA samples, a lower concentration of phosphoric acid was used during the solution-coating process (Table 1). These cathode materials were again made into half cells, formed at C/10, and then cycled between 2.8 and 4.4 V (Figure S2). The initial capacity of the TC-NMA and TC-BM-NMA increased compared to the C-NMA. The C-NMA and the TC-NMA had first cycle discharge capacities of 185 and 221 mA h/g, respectively. The initial capacities for the C-BM-NMA and the TC-BM-NMA were 205 and 223 mA h/g, respectively. However, these are still below the 234 mA h/g capacity obtained by the P-NMA. When comparing the coated samples, the TC-NMA has a capacity fade of 20% compared to a 27% fade in the TC-BM-NMA material. Both coated samples maintain a larger discharge capacity of above 4.0 V during the discharge with the P-NMA, TC-NMA, and TC-BM-NMA having 20, 47, and 36 mA h/g respectively, signaling that they maintain more of their hexagonal H3 phase.[42]

High-Voltage Tests. While the thinly coated NMA samples show a marked increase in capacity retention (Figure 7e), a final attempt was made to get the coated sample's initial capacity as near as possible to the pristine material. A final round of "ultra-thin- coated samples was made and tested at high voltages with the expectation that the ball-milled material, being pulverized or "pre-cracked", will maintain more of its capacity because most nickel-rich cathode cracking occurs at charge voltages >4.5 V (V vs Li/Li^+).[13,43] The P-NMA, UTC-NMA, and UTC-BM-NMA were first made into half coin cells and formed at C/10 between 2.8 and 4.4 V and then cycled at C/3 between 2.8 and 4.6 V (Figure 8). Here, most of the initial capacity of the P-NMA has been achieved by the UTC-NMA samples. After 100 cycles of C/3 charge to 4.6 V, the UTC-BM-NMA shows the highest capacity of 180 mA h/g followed by the UTC-NMA at 160 and P-NMA at 100 mA h/g. The lithium phosphate-coated samples provide significant protection against capacity fade and voltage decay. The ball-milled sample retains more of its capacity, has less voltage decay, and retains more of its discharge voltage plateau. Again, both coated samples maintain a larger discharge capacity of above 4.0 V during discharge with the P-NMA, UTC-NMA, and UTC-BM-NMA having 13, 39, and 40 mA h/g respectively. The fact that the UTC-BM-NMA has more >4.0 V voltage plateau than the UTC-NMA when cycled at high voltages compared to the moderate voltage window may mean the ball-milled material experiences less cathode cracking. However, the UTC-BM-NMA has a higher-than-expected capacity drop between C/10 and C/3 discharge, possibly due to its higher charge-transfer resistance (Figure 8). Changes in electrode

https://doi.org/10.1021/acsaem.2c00606
ACS Appl. Energy Mater. 2022, 5, 6996−7005

composition and processing should also be investigated but are beyond the scope of this research.

To understand the mechanism of lithium loss during the coating process, the three coatings' thicknesses can be compared. These cathode materials were made into either half cells or full cells and cycled between either 2.8−4.4 V in Gen-2. In general, the phosphate-coated samples have a lower initial capacity than the P-NMA. It is thought that the lower initial capacity that might be caused by lithium diffusion from the cathode particle to form the Li_3PO_4 film or the lowered capacity may simply be caused by lithium evaporation during the heating step of the coating process. To explore this, care was taken to limit the exposure of excess phosphoric acid by using varying concentrations of phosphoric acid during the solution process (Table 1) while maintaining the same heating temperature and time. The initial specific discharge capacity for the C-NMA, TC-NMA, and UTC-NMA were 185, 221, and 224 mA h/g, respectively. This suggests that the available lithium from the cathode particles, not only residual lithium species, can react with the phosphoric acid to create lithium phosphate and that excess phosphoric acid will consume lithium, lowering the cathode's initial capacity. Data from XPS suggests that LiOH is the residual lithium species preferentially consumed, so care must be taken to limit excess phosphoric acid from consuming electrochemically active lithium from the cathode particle once LiOH has been exhausted from the particle surface. Excess phosphoric acid will also consume active lithium before all the surface Li_2CO_3 is exhausted, both lowering initial discharge capacity and increasing surface film resistance (R_{sf}).

Full cells were used to test the coated and ball-milled material performance without the infinite lithium reservoir. NMA full coin cells were made using 90 wt % super P graphite. Cells were initially formed at 4.2 V (V vs graphite) at C/10 and were then charged to 4.3 and 4.4 V (V vs graphite) up to the 10th cycle. The cells were then charged and discharged at C/3, and the results can be seen in Figure 9. The full cell results follow the same pattern as the half cells, in that both the ball-milled and non-ball-milled samples show increased capacity retention when compared to the pristine material. The capacity retention after 100 cycles at C/3 for the P-NMA, UTC-NMA, and the UTC-BM_NMA samples were 36, 68, and 82%, respectively. In addition, the UTC-BM-NMA material shows virtually the same initial C/10 discharge capacity in full coin cells as the pristine material.

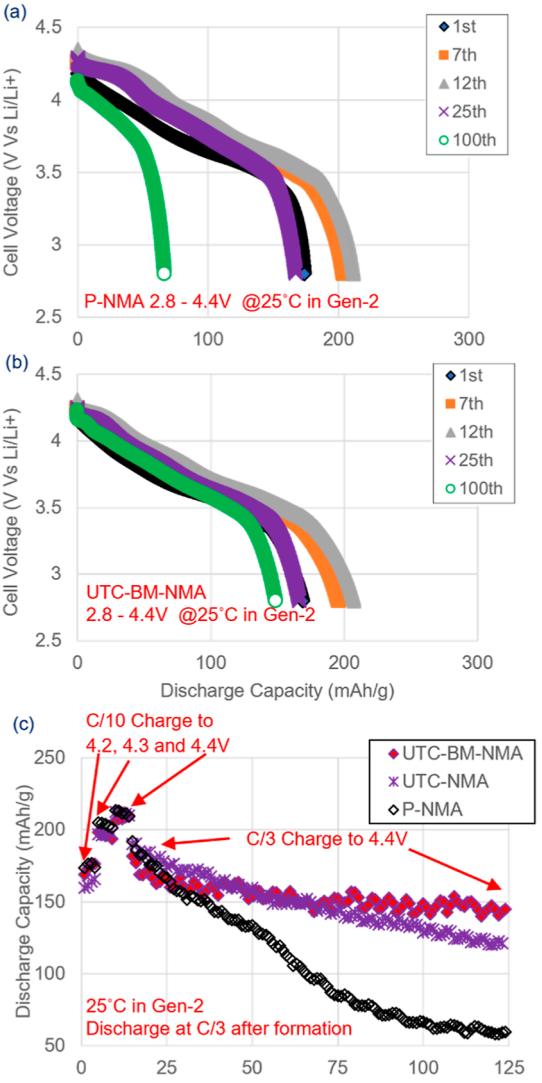

Figure 9. Full cell cycling data for P-NMA (a) and UTC-BM-NMA (b). The P-NMA and UTC-BM-NMA have the same discharge capacity when charged to 4.4 v (V vs graphite) and the UTC-BM-NMA retains more of its capacity after 100 cycles. Discharge capacity versus cycle number showing capacity retention of the coated and pristine NMA (c).

CONCLUSIONS

NMA cathode material's air stability has been increased with a lithium phosphate coating. Once coated, the electrode processing and handling may no longer require special handling in a dry room environment, significantly reducing the cost of manufacture. The cells have higher capacity retention and less voltage decay when the appropriate concentration of phosphoric acid is used to form a protective lithium phosphate coating. These concentration-dependent results are further improved by first pulverizing the NMA secondary particles into their individual primary constituents and performing the same surface treatment. These materials avoid secondary particle fracture and retain 40% more of their discharge capacity compared to the pristine material when charged at high voltages in full cells. Future work should focus on even thinner coatings to reduce the impedance at high charge/discharge rates, obtaining more conformal coatings, and electrode composition and processing studies using both ball-milled and pristine NMA as a bimodal system.

ASSOCIATED CONTENT

Supporting Information

The Supporting Information is available free of charge at https://pubs.acs.org/doi/10.1021/acsaem.2c00606.

Rietveld refinement data for pristine and ball-milled NMA, XRD data for pristine and ball-milled NMA, and half-cell cycling data for pristine, ball-milled, and thinly coated NMA (PDF)

AUTHOR INFORMATION

Corresponding Authors

Ryan Brow − *Center for Integrated Mobility Sciences, National Renewable Energy Laboratory, Golden, Colorado 80401, United States;* orcid.org/0000-0001-5984-2446; Email: Ryan.Brow@nrel.gov

https://doi.org/10.1021/acsaem.2c00606
ACS Appl. Energy Mater. 2022, 5, 6996−7005

Shriram Santhanagopalan − *Center for Integrated Mobility Sciences, National Renewable Energy Laboratory, Golden, Colorado 80401, United States;* orcid.org/0000-0003-4703-1341; Email: shriram.santhanagopalan@nrel.gov

Arumugam Manthiram − *Materials Science and Engineering Program and Texas Materials Institute, The University of Texas at Austin, Austin, Texas 78712, United States;* orcid.org/0000-0003-0237-9563; Email: manth@austin.utexas.edu

Authors

Anthony Donakowski − *Center for Integrated Mobility Sciences, National Renewable Energy Laboratory, Golden, Colorado 80401, United States*

Alex Mesnier − *Materials Science and Engineering Program and Texas Materials Institute, The University of Texas at Austin, Austin, Texas 78712, United States*

Drew J. Pereira − *Center for Integrated Mobility Sciences, National Renewable Energy Laboratory, Golden, Colorado 80401, United States*

K. Xerxes Steirer − *Department of Physics, Colorado School of Mines, Golden, Colorado 80401, United States;* orcid.org/0000-0001-6137-2105

Complete contact information is available at: https://pubs.acs.org/10.1021/acsaem.2c00606

Funding

Funding for this work provided by the U.S. DOE Office of Vehicle Technology Extreme Fast Charge Program, Program manager Peter Faguy is gratefully acknowledged (VTO.1.1.3.427). The authors acknowledge the support from the Assistant Secretary for Energy Efficiency and Renewable Energy, Office of Vehicle Technologies of the U.S. Department of Energy (award number DE-EE0008445).

Notes

The authors declare the following competing financial interest(s): One of the authors (A. M.) is a co-founder of TexPower, Inc., a start-up company focusing on cobalt-free cathode materials for lithium-based batteries.

■ ACKNOWLEDGMENTS

The research was performed in laboratories sponsored by the Department of Energy Office of Energy Efficiency and Renewable Energy, located at the National Renewable Energy Laboratory and the University of Texas at Austin. The U.S. Government retains and the publisher, by accepting the article for publication, acknowledges that the U.S. Government retains a nonexclusive, paid-up, irrevocable, worldwide license to publish or reproduce the published form of this work, or allow others to do so, for U.S. Government purposes. Special thanks to Noemi Leick for supporting the acquisition and discussion of the BET data and Andrew Norman for acquisition of the TEM data.

■ REFERENCES

(1) Manthiram, A. An Outlook on Lithium Ion Battery Technology. *ACS Cent. Sci.* **2017**, *3*, 1063−1069.

(2) Ziegler, M. S.; Trancik, J. E. Re-examining rates of lithium-ion battery technology improvement and cost decline. *Energy Environ. Sci.* **2021**, *14*, 1635−1651.

(3) Castelvecchi, D. Electric cars and batteries: how will the world produce enough? *Nature* **2021**, *596*, 336−339.

(4) Ensling, D.; Cherkashinin, G.; Schmid, S.; Bhuvaneswari, S.; Thissen, A.; Jaegermann, W. Nonrigid Band Behavior of the Electronic Structure of LiCoO2 Thin Film during Electrochemical Li Deintercalation. *Chem. Mater.* **2014**, *26*, 3948−3956.

(5) Chebiam, R. V.; Kannan, A. M.; Prado, F.; Manthiram, A. Comparison of the chemical stability of the high energy density cathodes of lithium-ion batteries. *Electrochem. Commun.* **2001**, *3*, 624−627.

(6) Olivetti, E. A.; Ceder, G.; Gaustad, G. G.; Fu, X. Lithium-Ion Battery Supply Chain Considerations: Analysis of Potential Bottlenecks in Critical Metals. *Joule* **2017**, *1*, 229−243.

(7) Greenwood, M.; Wentker, M.; Leker, J. A bottom-up performance and cost assessment of lithium-ion battery pouch cells utilizing nickel-rich cathode active materials and silicon-graphite composite anodes. *J. Power Sources Adv.* **2021**, *9*, 100055.

(8) Grey, C. P.; Hall, D. S. Prospects for lithium-ion batteries and beyond-a 2030 vision. *Nat. Commun.* **2020**, *11*, 6279.

(9) Chebiam, R. V.; Prado, F.; Manthiram, A. Comparison of the Chemical Stability of Li1−xCoO2 and Li1−xNi0.85Co0.15O2 Cathodes. *J. Solid State Chem.* **2002**, *163*, 5−9.

(10) Liu, C.; Neale, Z. G.; Cao, G. Understanding electrochemical potentials of cathode materials in rechargeable batteries. *Mater. Today* **2016**, *19*, 109−123.

(11) Manthiram, A. A reflection on lithium-ion battery cathode chemistry. *Nat. Commun.* **2020**, *11*, 1550.

(12) Ahmed, S.; Nelson, P. A.; Gallagher, K. G.; Susarla, N.; Dees, D. W. Cost and energy demand of producing nickel manganese cobalt cathode material for lithium ion batteries. *J. Power Sources* **2017**, *342*, 733−740.

(13) Sun, H.-H.; Manthiram, A. Impact of Microcrack Generation and Surface Degradation on a Nickel-Rich Layered Li[Ni0.9Co0.05Mn0.05]O2 Cathode for Lithium-Ion Batteries. *Chem. Mater.* **2017**, *29*, 8486−8493.

(14) Teichert, P.; Eshetu, G. G.; Jahnke, H.; Figgemeier, E. Degradation and Aging Routes of Ni-Rich Cathode Based Li-Ion Batteries. *Batteries* **2020**, *6*, 8.

(15) Yang, J.; Xia, Y. Suppressing the Phase Transition of the Layered Ni-Rich Oxide Cathode during High-Voltage Cycling by Introducing Low-Content Li2MnO3. *ACS Appl. Mater. Interfaces* **2016**, *8*, 1297−1308.

(16) Abraham, D. P.; Twesten, R. D.; Balasubramanian, M.; Petrov, I.; McBreen, J.; Amine, K. Surface changes on LiNi0.8Co0.2O2 particles during testing of high-power lithium-ion cells. *Electrochem. Commun.* **2002**, *4*, 620−625.

(17) Pouillerie, C.; Croguennec, L.; Delmas, C. The LixNi1−yMgyO2 (y=0.05, 0.10) system: structural modifications observed upon cycling. *Solid State Ionics* **2000**, *132*, 15−29.

(18) Jang, Y.-I.; Huang, B.; Wang, H.; Maskaly, G. R.; Ceder, G.; Sadoway, D. R.; Chiang, Y.-M.; Liu, H.; Tamura, H. Synthesis and characterization of LiAlyCo1−yO2 and LiAlyNi1−yO2. *J. Power Sources* **1999**, *81*−*82*, 589−593.

(19) Croguennec, L.; Suard, E.; Willmann, P.; Delmas, C. Structural and Electrochemical Characterization of the LiNi1-yTiyO2 Electrode Materials Obtained by Direct Solid-State Reactions. *Chem. Mater.* **2002**, *14*, 2149−2157.

(20) Li, L.; Xu, M.; Yao, Q.; Chen, Z.; Song, L.; Zhang, Z.; Gao, C.; Wang, P.; Yu, Z.; Lai, Y. Alleviating Surface Degradation of Nickel-Rich Layered Oxide Cathode Material by Encapsulating with Nanoscale Li-Ions/Electrons Superionic Conductors Hybrid Membrane for Advanced Li-Ion Batteries. *ACS Appl. Mater. Interfaces* **2016**, *8*, 30879−30889.

(21) Gao, H.; Maglia, F.; Lamp, P.; Amine, K.; Chen, Z. Mechanistic Study of Electrolyte Additives to Stabilize High-Voltage Cathode-Electrolyte Interface in Lithium-Ion Batteries. *ACS Appl. Mater. Interfaces* **2017**, *9*, 44542−44549.

(22) Jang, S. H.; Jung, K.; Yim, T. Silyl-group functionalized organic additive for high voltage Ni-rich cathode material. *Curr. Appl. Phys.* **2018**, *18*, 1345−1351.

(23) Song, W.; Harlow, J.; Logan, E.; Hebecker, H.; Coon, M.; Molino, L.; Johnson, M.; Dahn, J.; Metzger, M. A Systematic Study of Electrolyte Additives in Single Crystal and Bimodal LiNi0.8Mn0.1 Co0.1O2/Graphite Pouch Cells. *J. Electrochem. Soc.* **2021**, *168*, 090503.
(24) Lee, S.-H.; Lee, S.; Jin, B.-S.; Kim, H.-S. Optimized electrochemical performance of Ni rich LiNi0.91Co0.06Mn0.03O2 cathodes for high-energy lithium ion batteries. *Sci. Rep.* **2019**, *9*, 8901.
(25) Xu, X.; Huo, H.; Jian, J.; Wang, L.; Zhu, H.; Xu, S.; He, X.; Yin, G.; Du, C.; Sun, X. Radially Oriented Single-Crystal Primary Nanosheets Enable Ultrahigh Rate and Cycling Properties of LiNi 0.8 Co 0.1 Mn 0.1 O 2 Cathode Material for Lithium-Ion Batteries. *Adv. Energy Mater.* **2019**, *9*, 1803963.
(26) Mo, Y.; Guo, L.; Jin, H.; Du, B.; Cao, B.; Chen, Y.; Li, D.; Chen, Y. Building nickel-rich cathodes with large concentration gradient for high performance lithium-ion batteries. *J. Power Sources* **2020**, *468*, 228405.
(27) Song, D.; Hou, P.; Wang, X.; Shi, X.; Zhang, L. Understanding the Origin of Enhanced Performances in Core-Shell and Concentration-Gradient Layered Oxide Cathode Materials. *ACS Appl. Mater. Interfaces* **2015**, *7*, 12864−12872.
(28) Yan, P.; Zheng, J.; Liu, J.; Wang, B.; Cheng, X.; Zhang, Y.; Sun, X.; Wang, C.; Zhang, J.-G. Tailoring grain boundary structures and chemistry of Ni-rich layered cathodes for enhanced cycle stability of lithium-ion batteries. *Nat. Energy* **2018**, *3*, 600−605.
(29) Guo, Q.; Huang, J.; Liang, Z.; Potapenko, H.; Zhou, M.; Tang, X.; Zhong, S. The use of a single-crystal nickel-rich layered NCM cathode for excellent cycle performance of lithium-ion batteries. *New J. Chem.* **2021**, *45*, 3652−3659.
(30) Li, H.; Li, J.; Ma, X.; Dahn, J. R. Synthesis of Single Crystal LiNi0.6Mn0.2Co0.2O2with Enhanced Electrochemical Performance for Lithium Ion Batteries. *J. Electrochem. Soc.* **2018**, *165*, A1038−A1045.
(31) Li, W.; Lee, S.; Manthiram, A. High-Nickel NMA: A Cobalt-Free Alternative to NMC and NCA Cathodes for Lithium-Ion Batteries. *Adv. Mater.* **2020**, *32*, 2002718.
(32) Kim, S.-B.; Kim, S.-J.; Kim, C.-H.; Kim, W.-S.; Park, K.-W. Nanostructure cathode materials prepared by high-energy ball milling method. *Mater. Lett.* **2011**, *65*, 3313−3316.
(33) Jo, C.-H.; Cho, D.-H.; Noh, H.-J.; Yashiro, H.; Sun, Y.-K.; Myung, S. T. An effective method to reduce residual lithium compounds on Ni-rich Li[Ni0.6Co0.2Mn0.2]O2 active material using a phosphoric acid derived Li3PO4 nanolayer. *Nano Res.* **2015**, *8*, 1464−1479.
(34) Stein, M., IV; Chen, C.-F.; Mullings, M.; Jaime, D.; Zaleski, A.; Mukherjee, P. P.; Rhodes, C. P. Probing the Effect of High Energy Ball Milling on the Structure and Properties of LiNi1/3Mn1/3Co1/3O2 Cathodes for Li-Ion Batteries. *J. Electrochem. Energy Convers. Storage* **2016**, *13*, 031001.
(35) Pan, T.; Alvarado, J.; Zhu, J.; Yue, Y.; Xin, H. L.; Nordlund, D.; Lin, F.; Doeff, M. M. Structural Degradation of Layered Cathode Materials in Lithium-Ion Batteries Induced by Ball Milling. *J. Electrochem. Soc.* **2019**, *166*, A1964−A1971.
(36) Wang, B.; Chakoumakos, B. C.; Sales, B. C.; Kwak, B. S.; Bates, J. B. Synthesis, Crystal Structure, and Ionic Conductivity of a Polycrystalline Lithium Phosphorus Oxynitride with the γ-Li3PO4 Structure. *J. Solid State Chem.* **1995**, *115*, 313−323.
(37) Kuwata, N.; Iwagami, N.; Matsuda, Y.; Tanji, Y.; Kawamura, J. Thin Film Batteries with Li3PO4 Solid Electrolyte Fabricated by Pulsed Laser Deposition. *ECS Trans.* **2009**, *16*, 53−60.
(38) Cho, D.-H.; Jo, C.-H.; Cho, W.; Kim, Y.-J.; Yashiro, H.; Sun, Y.-K.; Myung, S.-T. Effect of Residual Lithium Compounds on Layer Ni-Rich Li[Ni0.7Mn0.3]O2. *J. Electrochem. Soc.* **2014**, *161*, A920−A926.
(39) Sahni, K.; Ashuri, M.; He, Q.; Sahore, R.; Bloom, I. D.; Liu, Y.; Kaduk, J. A.; Shaw, L. L. H3PO4 treatment to enhance the electrochemical properties of Li(Ni1/3Mn1/3Co1/3)O2 and Li-(Ni0.5Mn0.3Co0.2)O2 cathodes. *Electrochim. Acta* **2019**, *301*, 8−22.
(40) Meng, K.; Wang, Z.; Guo, H.; Li, X.; Wang, D. Improving the cycling performance of LiNi0.8Co0.1Mn0.1O2 by surface coating with Li2TiO3. *Electrochim. Acta* **2016**, *211*, 822−831.
(41) Waag, W.; Käbitz, S.; Sauer, D. U. Experimental investigation of the lithium-ion battery impedance characteristic at various conditions and aging states and its influence on the application. *Appl. Energy* **2013**, *102*, 885−897.
(42) Chen, J.; Yang, H.; Li, T.; Liu, C.; Tong, H.; Chen, J.; Liu, Z.; Xia, L.; Chen, Z.; Duan, J.; Li, L. The Effects of Reversibility of H2-H3 Phase Transition on Ni-Rich Layered Oxide Cathode for High-Energy Lithium-Ion Batteries. *Front. Chem.* **2019**, *7*, 500.
(43) Li, J.; Manthiram, A. A Comprehensive Analysis of the Interphasial and Structural Evolution over Long-Term Cycling of Ultrahigh-Nickel Cathodes in Lithium-Ion Batteries. *Adv. Energy Mater.* **2019**, *9*, 1902731.

https://doi.org/10.1021/acsaem.2c00606
ACS Appl. Energy Mater. 2022, 5, 6996−7005